

Supporting Information for

Cryo-ET suggests tubulin chaperones form a subset of microtubule lumenal particles with a role in maintaining neuronal microtubules

Saikat Chakraborty^{1,2*}, Antonio Martinez-Sanchez^{1,3,4}, Florian Beck^{1,5}, Mauricio Toro-Nahuelpan^{6,7}, In-Young Hwang⁸, Kyung-Min Noh⁸, Wolfgang Baumeister^{1*}, Julia Mahamid^{6,9}

¹Department of Molecular Structural Biology, Max Planck Institute of Biochemistry, Am Klopferspitz 18, Martinsried 82152, Germany

²Current Address: Division of Structural Biology, University of Oxford, Roosevelt Drive, Oxford, OX3 7BN, UK.

³Institute of Neuropathology & Cluster of Excellence "Multiscale Bioimaging: from Molecular Machines to Networks of Excitable Cells" (MBExC), University Medical Center Göttingen, 37075 Göttingen, Germany.

⁴Current Address: Dep. Information and Communications Engineering, University of Murcia, Campus de Espinardo, 30100 Murcia, Spain

⁵Research group CryoEM Technology, Max Planck Institute of Biochemistry, Am Klopferspitz 18, 82152 Martinsried, Germany

⁶Structural and Computational Biology unit, European Molecular Biology Laboratory, Meyerhofstrasse 1, 69117 Heidelberg, Germany

⁷Current address: Santiago GmbH & Co. KG, Willich, Germany.

⁸Genome Biology unit, European Molecular Biology Laboratory, Meyerhofstrasse 1, 69117 Heidelberg, Germany

⁹Cell Biology and Biophysics unit, European Molecular Biology Laboratory, Meyerhofstrasse 1, 69117 Heidelberg, Germany

Corresponding authors: Saikat Chakraborty, Wolfgang Baumeister, Julia Mahamid

Email: chakraborty@biochem.mpg.de, baumeist@biochem.mpg.de, julia.mahamid@embl.de

This PDF file includes:

SI Methods
Figures S1 to S11
Tables S1 to S2
Legends for Movies S1 to S5
SI References

Other supporting materials for this manuscript include the following:

Movies S1 to S5
MS data table

SI Methods:

Primary neuron culture and grid preparation

Rat hippocampal neurons were derived from embryonic rats (E17-21) in accordance with the procedures accepted by the Max-Planck Institute for Biochemistry. Briefly, the embryo tissue was dissected and minced in HBSS-HEPES buffer and trypsinized for 15-30 mins to collect hippocampal neurons as described previously (1). Collected neurons were washed with DMEM and 10% FBS (Invitrogen), and seeded on 4-well 35 mm dishes to a concentration of 5×10^5 cells/well each containing four poly-L-lysine coated R1/4 Au 200 mesh Quantifoil grids (Quantifoil Micro Tools). Cells were kept in an incubator at 37 °C and 5% CO₂ for ~4 h. Then, the grids were transferred to a culture dish containing pre-conditioned B27 medium. After 3 days from seeding, cytosine β -D-arabinofuranoside (Ara-C) (SIGMA, C1768) was added to the culture dish (final concentration 5 μ M) to stop glial cell duplication. Neurons were cultivated for 10–18 days *in vitro*. One third of the culture medium was exchanged once a week. Grids were plunge-frozen on day 12 using a Vitrobot Mark 4 (Thermo Fisher Scientific). The Vitrobot was set to 37°C, 90 % humidity, blot force 10, blot time of 10 s and 2 s drain time.

P19 cell culture, neuronal differentiation and grid preparation

Murine pluripotent P19 cells (DSMZ, ACC 316) were cultured in P19 growth medium (P19GM) containing alpha-MEM (Gibco, 12571063) supplemented with nucleosides, 10% (v/v) FBS (Thermo Fisher Scientific, 16000036), 100 mg/mL each of penicillin and streptomycin (Gibco, 15140122) at 37°C with 5% CO₂. Sample preparation on EM grids was essentially same as described before (2). Briefly, Pluripotent P19 cells were grown on plasma cleaned, UV sterilized gold Quantifoil grids (R2/1, Au 200 mesh grid) coated with additional 20 nm carbon. Cells were kept in an incubator overnight to allow adhesion, followed by vitrification by plunge freezing using a Vitrobot Mark 4 (Thermo Fisher Scientific). In all cases, the Vitrobot was set to 37°C, 95 % humidity, blot force 10, blot time of 10 s and 2 s drain time.

In order to analyze luminal particle entry to MT lumen, 15 μ M Nocodazole (Sigma-Aldrich, M1404) was added to pluripotent P19 cells grown on EM grids in cell culture media for 30 mins. Media containing Nocodazole was deposited and cells were washed with PBS three times to remove residual drug followed by addition of fresh media to induce fresh MT polymerization. Grids were vitrified after 15 mins of incubation.

Pluripotent P19 cells were induced to differentiate into neurons in induction medium (P19IM) containing 95% alpha-MEM and 5% FBS. Briefly, cells were collected after trypsinization with 0.05% trypsin and re-suspended in P19IM. Cells were then allowed to aggregate in a low binding petri-dish in presence of 0.5 μ M all-trans retinoic acid (RA) (SIGMA, R2625-50MG). Aggregates of

P19 cells formed within 2 days and further continued for another 2 days with fresh P19IM containing RA. Aggregates were then harvested and treated with 0.05% trypsin (Gibco, 25300054) and DNase (50 µg/mL) (New England Biolabs GmbH, M0303S) followed by resuspension in P19GM. Cells were plated in 35 mm poly-L-lysine-coated tissue culture dishes at a density of $\sim 5 \times 10^5$ cells/ml each containing four poly-L-lysine coated R2/1 Au Quantifoil 200 mesh grids. Ara-C (SIGMA, C1768) was added at 5 mM concentration after 2 days and culture continued for 7-10 days. Grids were vitrified between days 10-14.

hiPSCs culture, neuronal differentiation and grid preparation

Human iPSCs (male CESC-G-297) were derived from peripheral blood mononuclear cells following Institutional Review Board (IRB) approval and Stem Cell Research Oversight (SCRO) approval at Stanford University and under informed consent. hiPSCs were maintained below passage 40, regularly tested for mycoplasma (assayed with Mycoplasma PCR Detection Kit, iNtRON), and examined for genome integrity (using low coverage whole genome sequencing). hiPSCs were cultured in vitronectin (Thermo Fisher Scientific, A14700) coated dish (0.5 µg/cm²) with Essential 8 medium with supplement (Thermo Fisher Scientific, A1517001). For neuronal differentiation, we adapted and modified published methods that generate excitatory neurons using rapid Neurogenin-2 (NGN2) induction (3, 4). Briefly, hiPSCs were transduced with TetO-hNGN2-P2A-eGFP-T2A-PuroR and rtTA lentivirus at 60% of confluency (Day 0). After 24 h, the virus-containing medium was washed away and replaced with 1:1 ratio of Neurobasal A (Thermo Fisher Scientific, 10888022) and DMEM/F12 medium containing GlutaMAX, Insulin (Gibco, 51300-044), N2/B27 without Vitamin A (Thermo Fisher Scientific, 17502048/12587010) supplements, and 1 µg/ml of doxycycline to activate TetO promoter (Day 1). hiPSCs expressing hNGN2-P2A-eGFP-T2A-PuroR were selected by adding 3 µg/ml puromycin (Day 2) for 24 h. Cells were then dissociated with Accutase (Thermo Fisher Scientific, A1110501), counted, and re-plated in the triple coated dish containing EM grids described below (Day 3 - seeding), and maintained in Neurobasal medium (Thermo Fisher Scientific, 21103049) containing B-27 w/o Vitamin A (Gibco, 12587010), GlutaMAX (Thermo Fisher Scientific, 35050061), 200 µM of L-Ascorbic Acid (Sigma, A5960), 1 µM of DAPT (Tocris, 2634), 1 µg/ml puromycin, and 1 µg/ml doxycycline. The triple coating is composed of 0.1 mg/ml of Poly-D-Lysine (Sigma, P0899), 10 µg/ml of Laminin (Sigma, 11243217001), and 10 µg/ml of Fibronectin (Sigma, F0895). Cells were cultured for two more days with 1 µg/µl puromycin and 1 µg/ml doxycycline (Day 5). Half of the medium was changed every two days without puromycin and doxycycline until the induced neurons were vitrified (Day 9).

Lentivirus generation: two lentivirus plasmids from a published study (4), each containing hNGN2-P2A-eGFP-T2A-PuroR under the control of TetO promoter (Addgene 79823) and reverse tetracycline activator (rtTA) (Addgene 19780), were used to produce transgenes. Lentivirus was generated by co-transfecting transgene plasmid with two helper plasmids, pMD2 (Addgene 12259)

and psPAX2 (Addgene 12260), by calcium phosphate transfection kit (Takara, 631312) following the manufacturer's protocol into HEK293 cells. After 48-72 h of incubation, media containing lentiviruses were harvested and concentrated at 112,000 g for 3 h, aliquoted, and stored at -80°C.

EM Grid micro-patterning: gold (Au) 200-mesh grids with a holey 12 nm thick film made of SiO₂ (R1/4, hole size/spacing in µm, Quantifoil Micro Tools), were micro-patterned (5). Briefly, grids were plasma cleaned on both sides at 100 W power with a 10 cm³ per min flow rate of oxygen gas for 30–40 s (Diener Femto Plasma, DienerElectronic). Next, grids were incubated on droplets of poly-L-lysine grafted with polyethylene glycol (PLL(20)- g[3.5]-PEG(5), SuSoS AG) at a concentration of 0.5 mg/ml in 10 mM HEPES pH 7.4, for 1h at room temperature on parafilm in a humid chamber. Following passivation, the grids were blotted with filter paper from the back, allowed to dry for few seconds and immediately placed on a drop of PLPP (4-benzoylbenzyl-trimethylammonium chloride, 14.5 mg/ml) in a sealed glass bottom ibidi µ-Dish 35mm low (ibidi). Grids were immediately micro-patterned using a DMD-based illumination (Primo, Alvéole Lab), applying a dose of 1,500 mJ/mm². Grids were promptly retrieved from the PLPP solution, washed in a 1,000 µl drop of water and two consecutive washes in 300 µl drops of PBS supplemented with Ca and Mg. Patterned grids were stored wet in PBS supplemented with Ca²⁺ and Mg²⁺ at 4 °C in a humid chamber. For functionalization of the micropatterns, grids were incubated at room temperature for 30 min in a 20 µl drop of 50 µg/ml laminin (Sigma, 11243217001) and 50 µg/ml fibronectin (Thermo Fisher Scientific) in PBS supplemented with Ca and Mg. Grids were then washed three times in 300 µl drops of the corresponding buffer and stored at 4 °C in a humid chamber until use. hiPSC cells were seeded on laminin/fibronectin micro-patterned grids at a density of 2×10⁴ cells per cm² in a glass bottom ibidi µ-Dish 35mm high (ibidi), and incubated for 48 h in this dish. In parallel, another glass bottom ibidi µ-Dish 35mm high (ibidi) was seeded with 2×10⁵ cells per cm² (without grids). After 48 h, the grids were transferred (from the 2×10⁴ cells per cm² seeded dish) to the 2×10⁵ cells per cm² seeded dish. Neurons were grown for 6 days post-seeding with half-media change every 2 days. Grids were plunged on day 6 post-seeding using a Leica GP plunger (Leica Microsystems) at a 70% humidity and blotted for 1.5 sec, no nanogold fiducials were added.

Micropattern design: micropatterns were designed in Inkscape (<http://www.inkscape.org/>) as 8-bit binary files and exported as .png files, which can be loaded into the Leonardo software v.4.12 (Alvéole Lab). Neuronal circuits micropatterns used for hiPSCs were designed such that 10 µm circles were patterned at the center of the grid square to direct cell body attachment. Circles were connected alternately with straight or curly lines (10 µm wide) to facilitate extension of neuronal process. Micro-patterned circuit covered an area of 10 x 8 grid squares (in a 200-mesh grid).

HeLa cell culture, grid preparation and FIB micromachining

HeLa Kyoto cells Wild Type or expressing both C-terminally tagged green fluorescent protein (GFP)-β-tubulin and mCherry tagged histone (H2B-mCherry) were cultured at 37°C with 5% CO₂

in Dulbecco's modified Eagle's medium (DMEM) (Gibco, 31966021) containing 10% (v/v) fetal bovine serum (FBS) (Gibco, 16000036), 2 mM L-glutamine, 100 mg/mL penicillin, 100 mg/mL streptomycin, and 0.5 mg/mL geneticin (G418) (Gibco, 10131019). Sample preparations for cryo-ET follow similar steps as described for P19 cells (2).

For the preparation of mitotic HeLa cells, mitotically synchronized cells using thymidine (Sigma, T1895-5G) block followed by STLC treatment as described before (2) were detached from the culture flask by mechanical shake off, and the collected medium was centrifuged at 300 g for 2 min to concentrate the cell pellet. 4 μ L of the cell suspension was deposited onto plasma cleaned holey carbon-coated 200 mesh copper R 2/1 grids followed by vitrification by plunge freezing using a Vitrobot Mark 4 (Thermo Fisher Scientific) using similar conditions as in P19 sample preparation.

Plunge-frozen grids fixed into custom-made autogrids were mounted into a 45°-pre-tilted shuttle and micro-machined using a dual-beam (FIB/SEM) microscope (Quanta 3D FEG, FEI) as described before (2, 6). For improved conductivity of the final lamella, grids were sputter coated after cryo-FIB preparation with platinum in the Quorum prep-chamber (10 mA, 3 s).

Cryo-TEM and tomography

Tilt series were collected on a Titan Krios (Thermo Fisher Scientific) operated at 300 kV equipped with a field-emission gun, a Quantum post-column energy filter (Gatan) operated in the zero-loss mode using a 20-eV slit, a K2 Summit or K3 direct detector camera (Gatan) operated in counting mode, and a Volta phase plate (VPP) (Thermo Fisher Scientific) for part of the data. Alignment and operation of the Volta phase plate were essentially carried out as described by Fukuda et al. (7), applying a beam tilt of 10 mrad for autofocus. Data were recorded with SerialEM software (8). Only the best quality tomograms with good contrast produced from cellular areas thinner than 200 nm were used for image processing (**Table S1**).

Tilt series of primary neurons were acquired either with dose-symmetric (9) or asymmetric bi-directional tilt scheme and a nominal defocus ranging from 2 to 6 μ m at an EFTEM magnification of $\times 64,000$ resulting in pixel size at the specimen level of 2.24 Å. Total dose was kept under 100 e/Å². 60 tomograms were processed for subsequent structural analysis.

Tilt series of hiPSC-derived neurons were collected with dose symmetric scheme at an EFTEM magnification of $\times 64,000$ corresponding to pixel size at the specimen level of 2.129 Å, 2.5–4 μ m defocus, with constant dose for all tilts, total dose under 150 e/Å². Tilt-series were acquired with the VPP. 8 tomograms were processed for subsequent structural analysis.

A total of 46 bi-directional tilt-series corresponding to pluripotent control, Taxol-treated and Nocodazole-treated P19 cells was collected at $\times 42,000$ resulting in pixel size of 3.42 Å using VPP with a target defocus of 0-200 nm. A total of 35 dose-symmetric tilt series corresponding to

pluripotent and differentiated P19 cells was also collected with an EFTEM magnification of $\times 64,000$ corresponding to pixel size at the specimen level of 2.24 Å and 2-5 μm defocus. In all cases, cumulative dose ranged between 90-120 $\text{e}/\text{\AA}^2$.

HeLa cell tomograms were collected from FIB-milled lamellae at $\times 33,000$ resulting in pixel size of 4.21 Å using VPP with a target defocus of 0 nm as described previously (2).

Processing of tilt-series

For preprocessing of tilt series, the MATLAB based TOMOgram MANager (TOMOMAN; <https://github.com/williamnwan/TOMOMAN>) package was used (10). Frames were first sorted, followed by motion correction using MontionCor2 (11) with 3×3 patches. Bad frames were then omitted from the motion corrected stacks. Frames were exposure filtered according to their cumulative electron dose. Defocus parameters were determined using GCTF 1.06 (12) or CTFFIND 4.1.14 (13) on unfiltered stacks. For high resolution data processing, 3D defocus gradients in primary neuron and P19 tomograms were corrected using NovaCTF (14). CTF correction via phase-flipping used a Z-slab thickness of 15 nm. The resulting tomograms were consecutively binned via Fourier cropping. Preprocessing of hiPSC data was performed using Warp 1.7.b (15) including frame alignment, gain correction, dose filtering, tilt sorting, and CTF fitting. In-focus tomograms collected with VPP were not CTF corrected. In all cases, the dose-filtered stacks were aligned with patch tracking in the IMOD software package (16). Final alignment of the tilt-series images was performed using the linear interpolation option in IMOD without CTF correction. For tomographic reconstruction by back-projection, the radial filter options were left at their default values (cut off, 0.35; fall off, 0.05). Missing wedge compensated and denoised cross-section of the tomogram represented in **Fig. S1A** and **S1D** was prepared for visualization purpose using IsoNet (17).

MT tracing and curvature measurement

MT segmentations were performed with the automated module in Amira software v.6.2.0 (Thermo Fisher Scientific) as described before (2) in the IMOD reconstructed tomograms using a generic missing wedge-modulated hollow cylinder with outer and inner radii of 14 and 7 nm, respectively and 120 nm length as a template. The coordinates of the traced filaments were resampled in MATLAB (MathWorks) to obtain equidistant points. MT curvature was determined by measuring the tangent-correlation length as described in our previous work (2). Data analysis was done by fitting a linear regression line in Origin 9.2 (OriginLab, Northampton, MA) on the data points obtained from each tomogram. aL_p values were calculated from the inverse slopes of the linear regression lines. Goodness of fits were determined from the Adjusted- R^2 values. Only fits with Adj- $R^2 > 0.8$ are considered.

Density tracing and particle picking

For density tracing and particle picking, tomograms were smoothed by Gaussian low-pass filtering at $\sigma=0.5$ pixels and the MT lumen was segmented based on the MT centerline tracing. Densities within the lumen were traced in 3D using a discrete Morse theory based software package PySeg (https://github.com/anmartinezs/pyseg_system) (18). Briefly, grayscale minima positions were identified and the most relevant ones were preserved by topological persistence simplification, while discarding those generated from noise or spurious densities. Next, mean shift clustering method (19) with 6 nm bandwidth was applied that allowed detection of particles and particle picking within the MT lumen in an unbiased template-free manner. The persistence threshold was set for picking all luminal particles independent of the type of density. Therefore, this threshold was adjusted for having the same density of minima at the shell for every MT, specifically 0.004 vertices/nm³ for phase plate tomograms and 0.006 vertices/nm³ for the defocus tomograms.

Subtomogram averaging of luminal particles

MTs were segmented using the filament-tracing module in Amira v.6.2.0, (Thermo Fisher Scientific), and luminal particles picked as described above. Subtomogram analysis was performed using RELION (v.3.0.5) following published protocols (20). During the refinement, particle half-sets were processed independently. Unless stated explicitly, all refinements were performed *de novo*, that is, without the use of external references. Datasets corresponding to different cell types were processed separately (**Table S1**).

Luminal particle subtomograms from the coordinates determined by the automated particle picking algorithm were extracted at 1x binning (2.24 Å/pix for primary neurons, pluripotent P19 and P19-driven neuronal samples, except 2.129 Å/pix in case of hiPSC data and 4.21 Å/pix for mitotic HeLa samples) within a box size of 128 pixels³. For VPP data corresponding to P19 and HeLa, no CTF correction was performed and luminal particle subtomograms were reconstructed using IMOD (16) (3.42 Å/pix and 4.21 Å/pix, respectively) within a box size of 128 pixels³. For P19 cell data, we combined VPP datasets from different conditions to increase the particle number and improve angular sampling. All the subtomograms corresponded to side views only and lacked views from cross-sections. Nevertheless, individual particles having different orientation within the MT lumen helped mitigate this problem.

Here, the STA procedure for primary neuronal sample is described. All other samples were analyzed using the same strategy. 50,910 subtomograms were first combined with randomized Euler angle resulting in a sphere (**Fig. S3**, top left) and auto-refined in RELION (20) with global search to shift them to a common origin (**Fig. S3**, top right) using a soft cylindrical mask. This initial model was used as an input for 3D classification with a global spherical mask (130 Å diameter). In order to resolve heterogeneity in the dataset, a multi-tier (at least three) and exhaustive classification strategy was used. For the first classification step, particle alignment was skipped and

large numbers of classes (>20) were used to pick up small differences. Based on the classification, subtomograms were sorted and 3D auto-refined using global search parameters to generate class averages. In the second classification step, refined class averages from the first classification run were used as input (**Fig. S3**) with similar classification settings as in the previous run. We followed this procedure sequentially until no new classes were obtained from the refined class averages of the previous run. The classes that did not produce any new structure were taken as the final 'pure' class averages. Multiple different classification runs were performed using different RELION (20) optimization parameters (class numbers 5–25, T values 1–8, limit resolution E-step 8–12 Å) for comparison. A number of classes was consistently recovered, and only those were chosen for further validation. Similarity between the class averages was apparent (containing a ring-like density), although differences were observed in the orientation and position of the small globular densities on the ring. Therefore, the class averages were not mixed and treated as separate classes.

For further validation of the classification procedure, the entire neuronal dataset was divided into 6 subsets based on the acquisition date, and processed individually as described above. All reported classes were retrieved from these subsets.

The small size of the complexes and low resolution could introduce starting model bias, as well as produce non-optimum refinement solutions. Therefore, subsequent validation runs were performed for each 'pure' class average to check whether similar structures are obtained when a featureless soft-edged sphere or a cylinder were used as starting model instead of the corresponding particle average (**Fig. S3, S4B-D**). If refinement converged to a similar structure, the class average was taken to represent an optimum-refinement solution and largely free of heterogeneity. In order to assess similarity between classes, we calculated cross-correlations between the final solutions obtained from the particle average as starting model and those obtained from simple sphere and/or cylinder in Chimera (v.1.15) (**Fig. S4B-D**) (21). Cross-correlations were obtained using the 'fit' command in the command line and further refined using 'fit in map' from the menu.

Finally, the class averages were locally refined using a soft particle mask and post processed to determine gold standard FSC curve.

Particle concentration measurements

Overall luminal particle concentrations present in different neuronal samples were measured by counting traced particles obtained by PySeg (18) per μm^3 of MT luminal volume. Prior to counting all particles, coordinates were refined in RELION (20). Following our rigorous 3D-classification method described above, concentrations of the individual class averages in their respective samples were determined by mapping them back into their MT of origin followed by counting their occurrences in each MT across tomograms belonging to a particular cell-type or condition and

converting them into mean number of particles/ μm^3 of luminal volume. The whole process was done semi-automatically. In all cases, lumen radius was set to 6 nm and MT length was obtained from the segmentations. MTs with length less than 100 nm were excluded from the analysis.

Subtomogram averaging and polarity determination of MTs

Resampled coordinates of the primary neuronal MTs extracted from Amira were used to make a tubular grid in MATLAB by placing points on each tubulin subunit taking into account inter-subunit distance of 40 Å along the filament z-axis and 60 Å around the helix. These positions were oversampled 2x-times and subtomograms were extracted from these grid points. Subtomograms extracted from the same filament were assigned a class number which helped in determination of MT polarity. Subtomogram averaging was performed in STOPGAP (22, 23). An initial reference was generated *de novo* from a single MT filament. 10,076 subtomograms were extracted from the oversampled positions using a binning factor of 2 (8.96 Å/pixel) and a box size of 64 pixels³, and a starting reference was generated by averaging all subtomograms. Due to in-plane randomization, the initial average resembled a featureless cylinder. Several rounds of alignment of the in-plane angle were conducted. Shift refinements were limited to 4 and 6 nm in x- and y- direction along the filament centerline. This averaging approach resulted in the emergence of the helical pattern of the MT (inset: **Fig. S1B, E**). We used this optimized starting model for refining the whole dataset for 5-6 iterations sequentially at bin4, bin2, and the unbinned data. In order to determine the polarity of the MTs, each MT in the dataset was averaged separately using multiclass averaging and subtomogram orientations were visualized in Chimera as lattice maps using the 'place object' plugin (24). Polarities were sorted out using visual inspection of the pF skew and followed by 180° change of the in-plane angles in the motive list. Finally, 34,906 unbinned subtomograms from 19 MTs (in two tomograms) were extracted using a box size of 96³ pixels³ and aligned iteratively, resulting in a refined map of a MT at a resolution of 8.19 Å.

In order to validate the density map, we used Chimera (21) to rigid body fit a tubulin dimer (PDB: 6dpv) into the obtained in-cell MT map, following the protocol described in (25, 26). First, the atomic model was translated up and down and rotated around its axis along the central pF. The alpha-helices in the map provided a strong constraint in placing the atomic model with more precision. A single orientation and position of the model produced the highest cross-correlation (CC) of 0.94. This fit further corroborates the determination of pF polarity in the density map. Visual inspection indicated suboptimal fit of a few alpha-helices. Therefore, a molecular dynamics flexible fitting protocol in qwikMD (27) with default parameters was used to refine the fitting of the tubulin dimer that is represented in Fig. 1H. Notably, the resolution was not enough to pin point α - and β -tubulin subunits in the density map.

Mass measurement of luminal particles

The luminal particles with a voxel size of 2.24/3.42 Å were filtered using a circular kernel (TomToolbox, tom_filter kernel=6) (28). The threshold for binarization was determined by measuring the mass of the ribosome particles from the same tomogram as described in literature (29). The threshold was decreased until the mean mass of all ribosome particles was ~3.6 MDa, (30) and then applied to the luminal particles for binarization. To correct for the different contrast regimes, a fudge factor of 0.5 was applied to the threshold. Binarized luminal particles were segmented using MATLAB's regionprops3, yielding the number of voxels for the biggest object inside one subvolume. The corresponding mass of each particle was calculated based on voxel size and the protein density (1.3 g cm⁻³).

Template matching and subtomogram averaging of ribosomes

To generate a subtomogram average of the ribosomes present in the primary neurons and P19 cells, ribosomes were localized by template matching in PyTom (31). As a template, we used the 4 nm down filtered structures of 80S ribosome (EMD: 1480) rescaled to the tomogram pixel size. False positives were identified by constrained cross-correlation (CCC) histogram which showed well separated peaks for the true and false positives (**Fig. S5C**). However, picked positions were also manually verified. In case of P19 ribosomes, 5553 (unbinned, 3.42 Å pixel size) subtomograms were extracted at the detected coordinates with their third Euler angle randomized and refined in RELION (20), which converged into a ribosome density (**Fig. S5D**). Particles were next sorted in 3D classification steps in RELION to remove remaining false positives. After final refinement and post processing, we obtained a density map at ~18 Å resolution (**Fig. S5E**) from 4723 particles. In case of neuronal ribosomes, 975 4x binned subtomograms centered on the identified coordinates were extracted and refined in RELION using a data-driven template. The refinement converged into a ribosome density. The data was further classified to remove false positives. All the good classes were combined and un-binned sequentially to 2x and 1x and final refinement gave 28 Å resolution ribosome average.

Polyribosome detection

Polyribosome detection was essentially based on hierarchical transformation clustering as described recently in Jiang et al. (32). The algorithm considered the directions of the transformations (rotations and translations). The method consists of 3 major steps: (i) transformations (rotations, translations) between ribosome pairs were calculated; (ii) distance matrices for rotations and translations were computed and combined; (iii) transformations were clustered based on the combined distance matrix (**Fig. S5G-I**).

Heat Maps of luminal particle micro-clustering

Heat Maps (**Fig. 6G, 6J**) were calculated by generating a volume of zeros with the size of the analyzed tomograms (928x928x500 voxels). For each particle position, the voxel value in the empty volume was set to 1. The 3D heat map was calculated by moving a spherical kernel with 2x radius of the particle over the volume. The mean for each kernel position was determined. Finally, the 3D heat map was projected in z.

Spatial statistics of luminal particle organization

We computed 1st order (NN-distance) and 2nd order univariate (Ripley's L) functions for spatial statistical analysis of 3D organization of luminal particles in a cellular compartment (MT lumen) as proposed in (18). NN-distance is based on the distance to the closest point from other points, whereas Ripley's L function takes into account distances between all pairs of points while evaluating the distribution at different length scales. The detailed description of the numerical corrections needed for successful computation of these functions from cryo-ET data is described in Martinez-Sanchez et al. (33). Protein localizations, angular orientations and 3D shapes were obtained from STA, MTs lumen were segmented from the traced MT centerlines and assuming a radius section of 6 nm. Complete Spatial Randomness with Volume exclusion synthetic patterns (CSRv) were used as null-models. In all cases, we simulated 20 instances for each MT to construct the interval of confidences for null-models. One-sided Welch tests were used to discard the next null-hypothesis: experimental particle density has the same mean as the CSRv case at a specific distance to a reference point (MT plus end or breakpoint).

Statistical analysis

Statistical analyses were performed with Origin 9.2. All boxes in the box-plot representations are bound by the 25th–75th percentile, whiskers span 5th to 95th percentile. Mean values were marked by a black box. Box plots are embedded inside a violin which indicate the distribution of the data. For statistical significance, nonparametric Mann-Whitney tests were performed unless stated otherwise. Significances were indicated by stars where ** indicated $p < 0.01$.

Visualization and Rigid body fitting

RELION post-processing were used to calculate FSC and perform B factor sharpening. UCSF Chimera (21) and ChimeraX (34) were used for visualization and figure generation. Numerical data and statistics were analyzed in Origin software. Quantification and plots were done in MATLAB (R2015b, The Mathworks, Inc. Massachusetts, USA). Membrane segmentations were performed with MemBrain-seg (35). Particle picking and density tracing were visualized using Paraview. Molecular model fitting was performed in Chimera (21). For rigid body fitting, yeast Cse1p (PDB:1Z3H) (36) filtered to 25 Å was used to represent the TBCD as described in (37). Models were fit into non-segmented density maps using the fit command from the command line in an

unbiased manner. Since TBCD model is the largest and has distinct shape, it was always fitted first and the rest were fitted sequentially. The 30 most probable fits were obtained. Highest cross-correlation hits were selected and refined using 'fit in map' command from the menu. For TBCE density map, globular heads were fitted with the Cap-Gly (PDB: 1WHG) (38) and UBL domains (PDB: 4ICV) (39), while the curved segment fitted with TLR4 (PDB: 3RJ0) (40) using similar rigid body fitting protocol.

Affinity purification and Mass spectrometry (AP-MS) based proteomics

HeLa Kyoto cells expressing GFP-tagged β -tubulin from BAC transgenes (41) were grown to near-confluency on two 15-cm cell culture dishes per interaction experiment. DSS (Thermo Fisher Scientific, 21555) solution was prepared fresh in dry DMSO at a concentration of 20 mM. Before crosslinking, cells were washed with ice-cold PBS (pH 8.0) to remove amine-containing culture media and extracellular proteins. DSS solution was added at a final concentration of 5 mM for 30 mins. The reaction was quenched by 10 mM Tris-Cl for 15 mins at room temperature. Cells were collected by scraping and snap frozen in liquid N₂. Three replicates were harvested. Cell pellets were lysed with a buffer containing 0.1% NP-40 (Sigma) and subjected to affinity purification using anti-GFP antibodies immobilized on a magnetic bead (Miltenyi Biotec, 130-091-125). Purified proteins were digested sequentially with LysC and trypsin, desalted and subjected to mass spectrometric analysis on an Orbitrap instrument (Q Exactive HF) at the mass spectrometry facility of Max-Planck institute of biochemistry. Raw files were processed with MaxQuant (42). MaxQuant output data was processed in Perseus (v.1.6.14.0) program with standard procedure (43). Protein identifications were filtered, removing hits to the reverse decoy database as well as proteins only identified by modified peptides. Protein LFQ intensities were logarithmized and missing values imputed by values simulating noise around the detection limit.

Protein structure and disorder prediction

Secondary structure of the AP-MS hits were predicted using Alpha-Fold2 (44). Protein disorder was predicted using the IUPred3 webserver (45). Both Alpha-Fold2 and IUPred3 predicted disorder in the same regions.

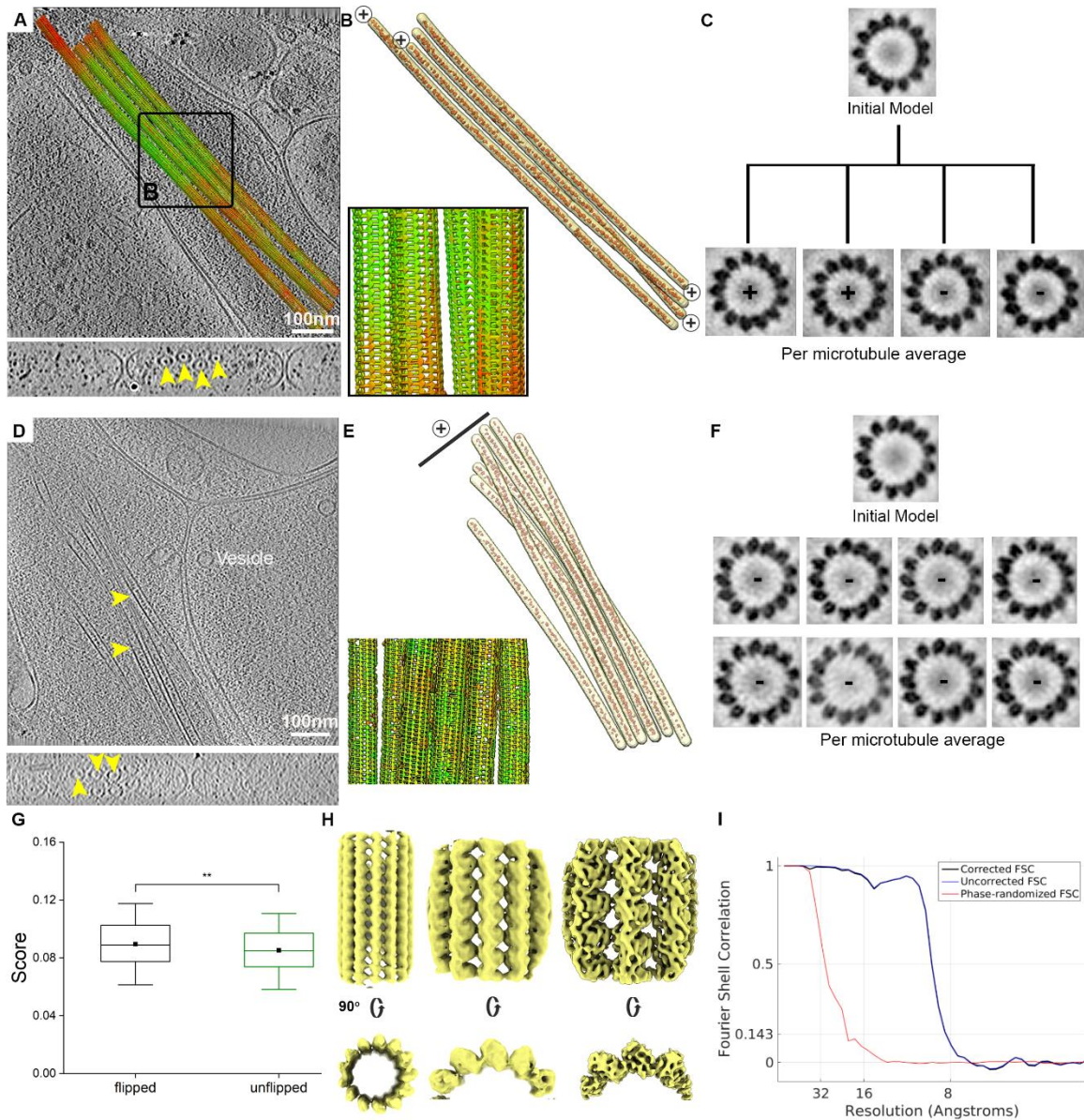


Fig. S1: Determination of MT polarity and structure exemplified in primary neuron processes. **A.** top: 9 nm x-y tomographic slice of a primary neuronal process containing 4 MTs superimposed with lattice map following STA (Methods, also shown in Figure 1A). Green indicates high cross correlation (CC)-values, whereas orange and red indicate lower CC-values. Bottom: missing wedge compensated, denoised cross-section view shows centrally located luminal particles (x-z slice; arrowheads). **B.** Segmented MTs with polarity assigned based on the description in C. Bottom left: zoomed in image of the lattice map within the black box in (A) showing different orientations of the subtomograms (represented as arrows). **C.** Individually averaged MTs displaying different polarities indicated by plus/minus sign based on the skew of the tubulin subunits. **D-F.** same as in (A-C) but showing a process with MTs that have uniform polarity. **G.** Comparison of scores before and after polarity flipping based on multiclass averaging. Mean value

439 indicated by black dot. Error bar indicates standard error. Statistical significance $**p < 0.01$, obtained
440 by nonparametric Mann-Whitney test. Data is representative, shown for one exemplary tomogram.
441 **H.** Left to Right: subtomogram averages of the neuronal MT at 4x binning, 2x binning and un-binned
442 resolution (pixel size 2.24Å). **I.** Fourier Shell Correlation (FSC) plot of the un-binned subtomogram
443 average obtained using 34906 subtomograms from three tomograms.

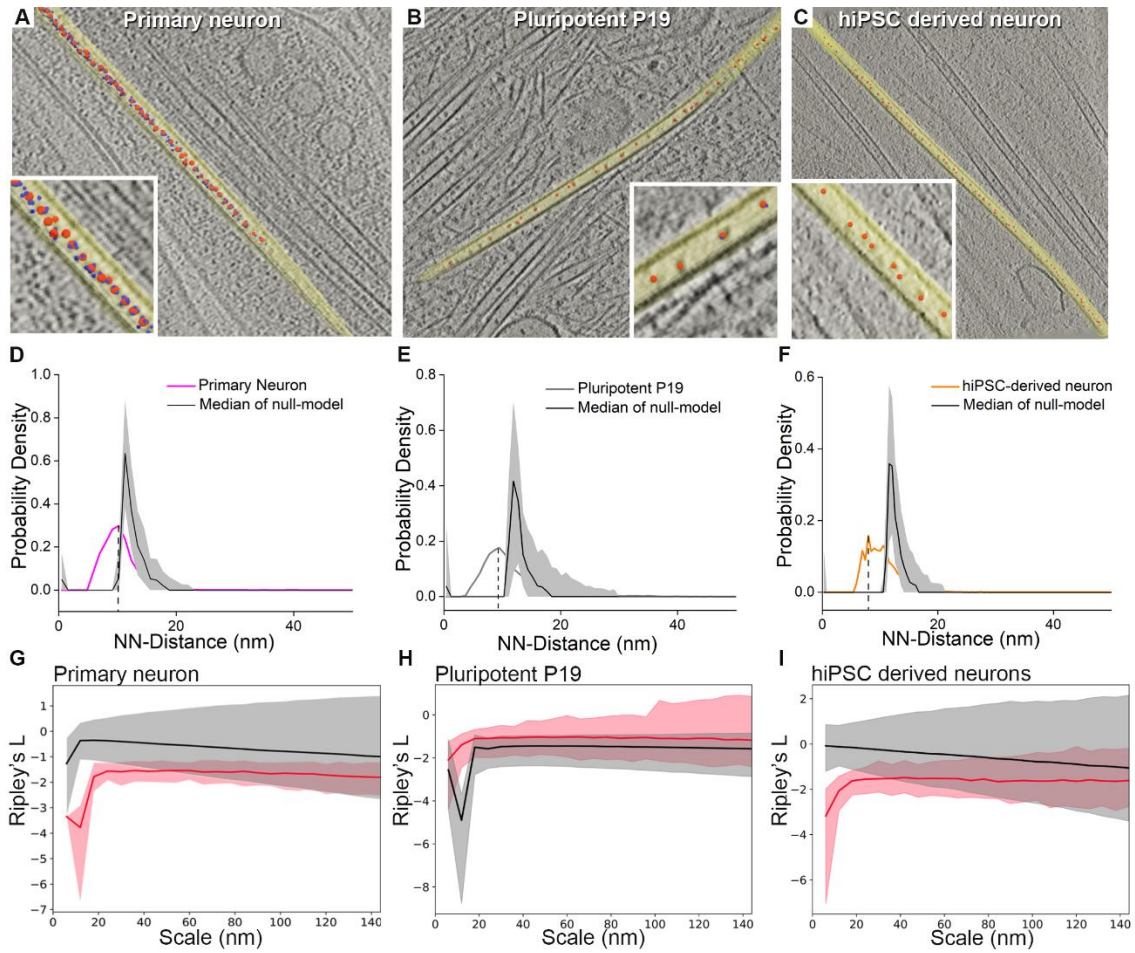


Fig. S2: Template-free detection, picking and spatial analysis of luminal particles. **A.** 9 nm thick tomographic slice of a primary neuron. Small blue spheres represent local minima obtained after topological simplifications (18), and red spheres are the final picking points representing mean shift clustering centers. Inset shows zoomed in image of the same. **B.** 6.8 nm thick tomographic slice of a pluripotent P19 cell. Red dots show detected particles after topological persistence simplifications and mean-shift clustering. Inset shows zoomed in image. **C.** Same as in (B) for hiPSC-derived neurons, slice thickness 4.25 nm. **D-F.** NN-distance distributions of luminal particles in the indicated cell-types. Null-model simulations (SI Appendix) representing complete spatial randomness are shown in black and shaded gray regions indicate interval of confidence (IC) [5, 95] %. Dashed vertical black lines indicate the most frequent nearest-neighbor distances in the data. **G-I.** Univariate 2nd order Ripley's L showing uniform distribution (SI Appendix) of luminal particles within MTs of the different cell-types. Solid lines indicate medians of the Ripley's L function for the experimental (Red) and simulated (black) random distribution, respectively. Shaded areas define the IC [5, 95] %.

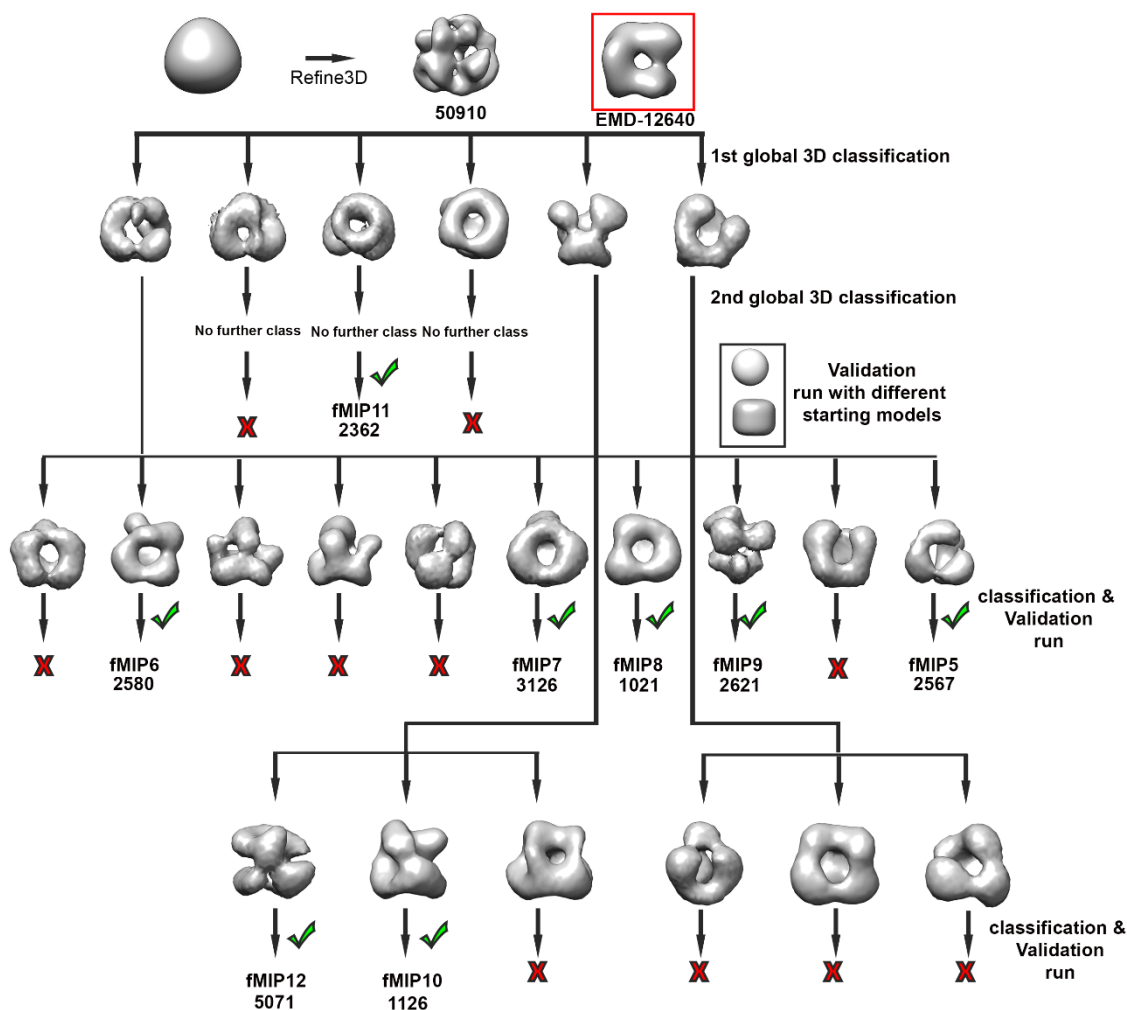


Fig. S3: Subtomogram averaging and classification workflow of luminal particles exemplified for primary neuronal cells. A similar workflow was used for the analysis of MT luminal particles in all cell types. The initial model (top left) was generated by averaging all picked particles with randomized orientations resulting in sphere-like structure. This initial average was 3D-autorefined in RELION (top middle), followed by 3D classifications. Density map obtained by Foster et al. (46) is shown in a red box for comparison (top left), but was not used in the processing. Classification was done sequentially, i.e. outputs of previous classification were used as input for a new round of classification until no new classes were obtained. The obtained class averages were validated for model bias, remaining heterogeneity and optimum-refinement (47) using soft-edged featureless geometric objects (sphere and/or cylinder) as starting references (box; shown on the left): for each class average, the corresponding particle list was used for two more independent auto-refinements with sphere and cylindrical starting models. If similar structures were produced in the separate refinements, indicating no model-bias and optimum refinement solution, the class average was accepted (green tick; similarity comparison also exemplified in Fig.S4 B-D).

474 Number of particles in each class average is indicated below the accepted average. Number of
475 tomograms, subtomograms and identified classes for each cell-type are provided in Table S1.

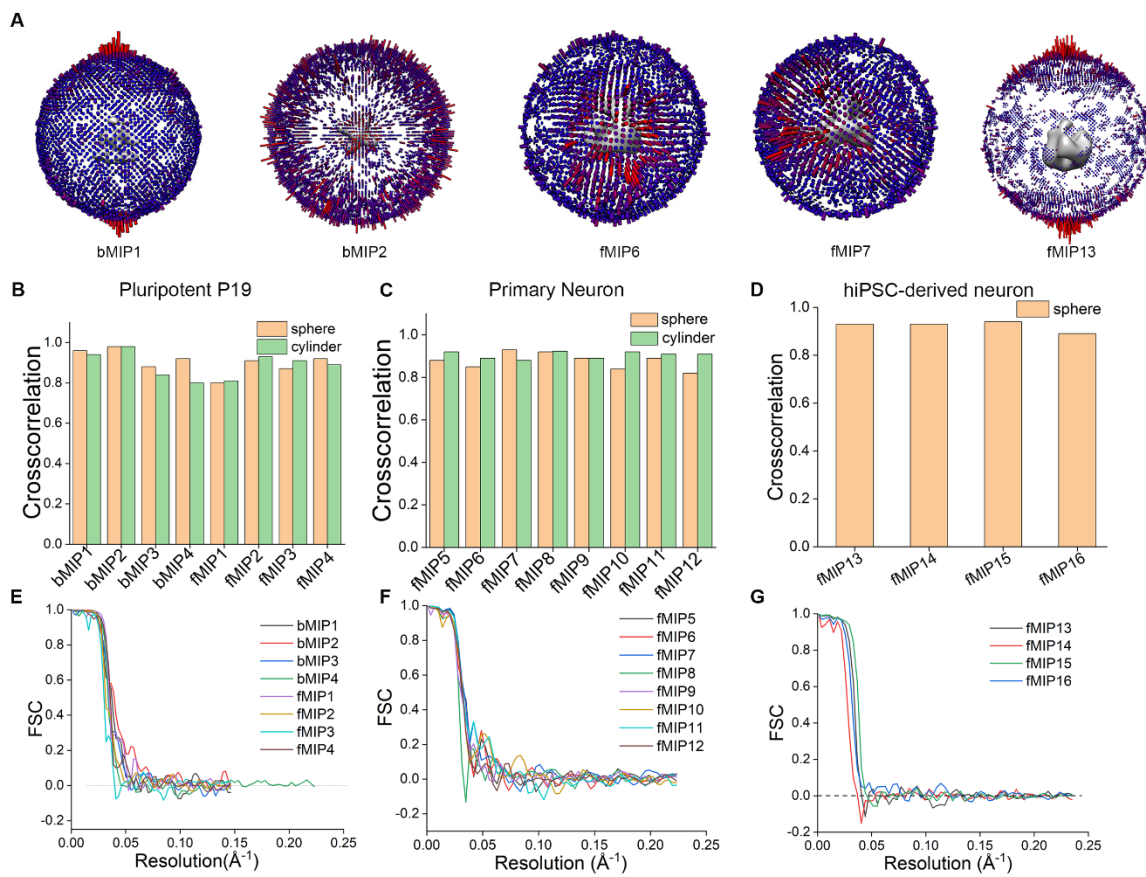


Fig. S4: Validation of STA-generated luminal particle maps from various cell-types. A. Angular distributions obtained from the averages for representative cases. Among all the reported averages, fMIP13 shows modest orientation bias. **B-D.** Similarity between the maps obtained from the refinements with the corresponding class averages as starting model and those obtained from simple featureless sphere and/or cylinder, evaluated using cross-correlation coefficient in Chimera for **B)** pluripotent P19 cells, **C)** primary neuron and **D)** hiPSC-derived neurons. **E-G.** FSC curves of the post-processed averages from **E)** pluripotent P19 cells, **F)** primary neuron and **G)** hiPSC-derived neuronal samples.

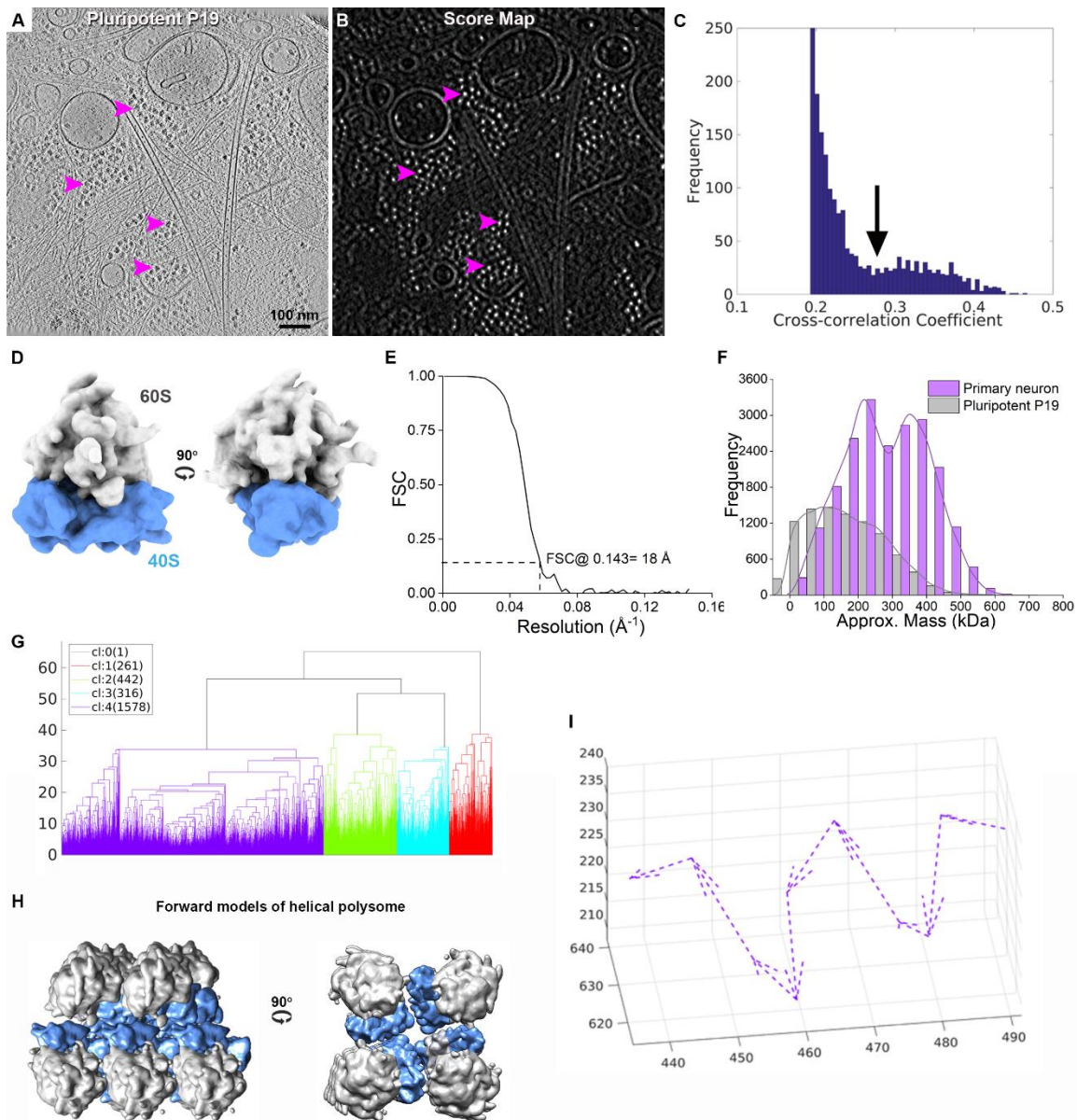


Fig. S5: Template matching, STA and organization of cellular ribosomes. **A.** 6.8 nm tomographic slice of a pluripotent P19 cell cytoplasm. Examples of ribosomes are indicated by violet arrowheads. **B.** Cross-correlation score map of the same tomogram following template matching (SI Appendix). Bright spots indicate high scores. Same ribosome clusters as in A are indicated by violet arrowheads. **C.** Histogram of cross-correlation coefficients (CCC) obtained after template matching. Bimodal distribution indicates false positives (low CCC) and real hits. Black arrow indicates cut-off value chosen to eliminate false positives. **D.** Density map of 80S murine ribosome obtained from 4723 particles by STA in RELION. Large (60S, grey) and small (40S, blue) subunits are indicated. **E.** FSC curve of the 80S ribosome average obtained after RELION post-processing. **F.** Histogram showing approximate mass distributions of the luminal particles of the indicated samples calculated from the corresponding tomograms. Particle mass was measured

496 using isosurface threshold that corresponds to the molecular weight of the 80S ribosome particles
497 present in the same tomograms. Lines indicate fit to the data distribution. **G.** Hierarchical clustering
498 of transformations of distance matrices calculated from rotations and translations between
499 ribosome pairs. **H.** Representative helical polysome class corresponding to largest cluster (purple)
500 in (G). 60S subunits (gray) face the cytosol. **I.** Vector diagram shows longest helical polysome
501 traced. Arrows indicate translations from n to n+1 ribosome. Axis unit is in pixels, 1 pixel = 3.42 Å.

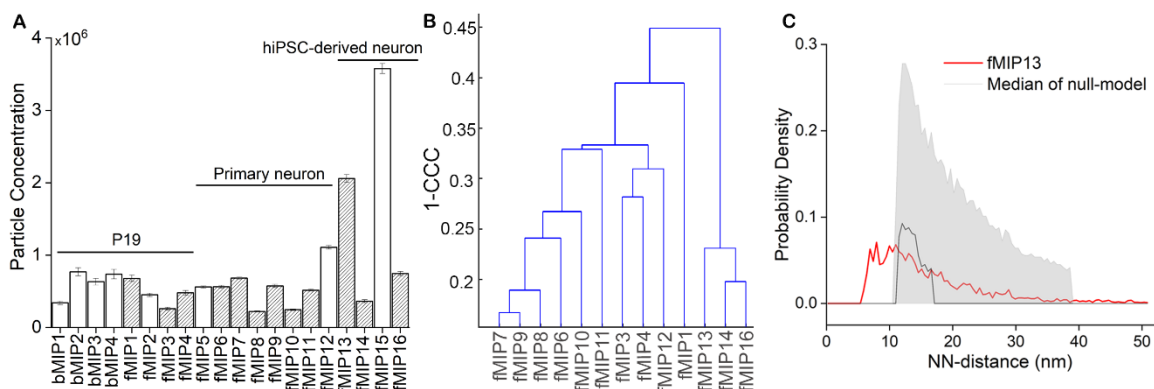


Fig. S6: Luminal particle abundances and their structural similarity. **A.** Concentrations (particles/ μm^3 of luminal volume) of the various class averages obtained from pluripotent P19 cells, primary neuron and hiPSC-derived neuron as indicated. Error bar indicates SEM. Gray bars correspond to the ring-like scaffold containing fMIPs found in all analyzed cell-types. Number of tomograms, subtomograms and identified classes for each cell-type are provided in Table S1. **B.** Hierarchical clustering tree of the ring-containing fMIPs. All ring-like scaffold containing density maps might represent complexes with variable compositions assembled on the ring-scaffold, or different conformations, determination of which is nontrivial at the obtained low resolution. Therefore, all indicated fMIPs (grey bars) were aligned on the ring-scaffold using rigid-body fitting. Pair-wise cross-correlation values were calculated among all the fMIPs with a limited angular search, and evaluated using a hierarchical clustering. Cluster tree shows classes of fMIPs branching only at high CCC values indicating structural similarity. **C.** NN-distance distribution of indicated class average in hiPSC-derived neurons. Null-model simulations (SI Appendix) representing complete spatial randomness are shown in black and shaded gray regions indicate IC [5, 95] %.

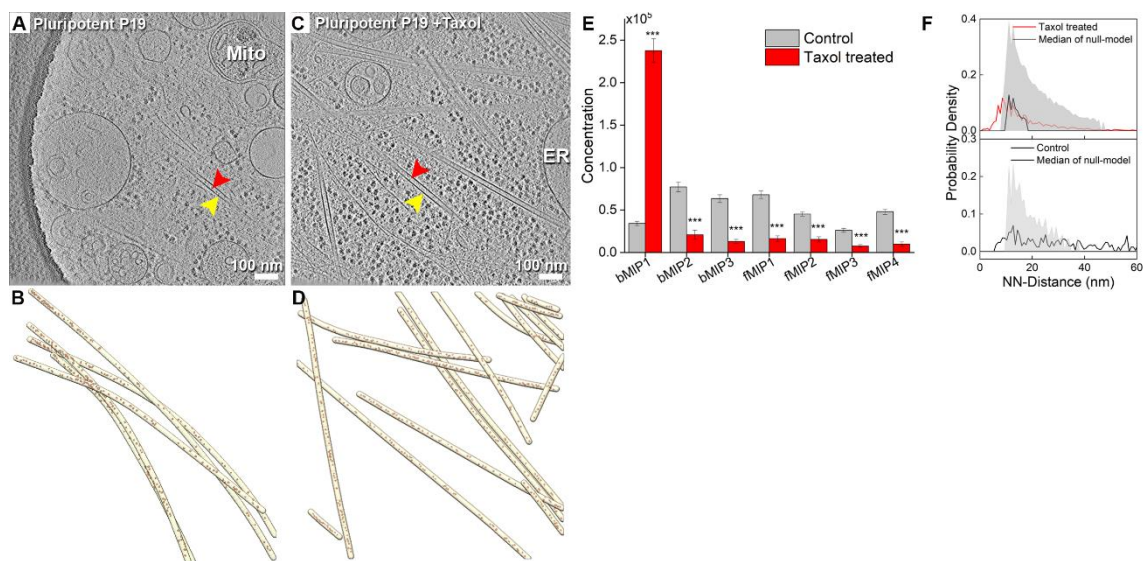


Fig. S7. Effect of Taxol on luminal particle abundance in pluripotent P19 cells. A-D. Tomographic slices (top row) and 3D-surface rendered (bottom row) MTs (yellow) and luminal particles (red) of control and Taxol-treated pluripotent P19 cell, slice thickness 6.8 nm. **E.** Concentrations (particles/ μm^3 of luminal volume) of the class averages in control and Taxol treated pluripotent P19 cells. Error bar indicates standard error of mean (SEM). Statistical significance ***p<0.001, obtained by two-sample t-test. **F.** NN-distance distribution of bMIP1 in control and Taxol-treated pluripotent P19 cells. Null-model simulations representing complete spatial randomness are shown in black and shaded gray regions indicate IC [5, 95] %.

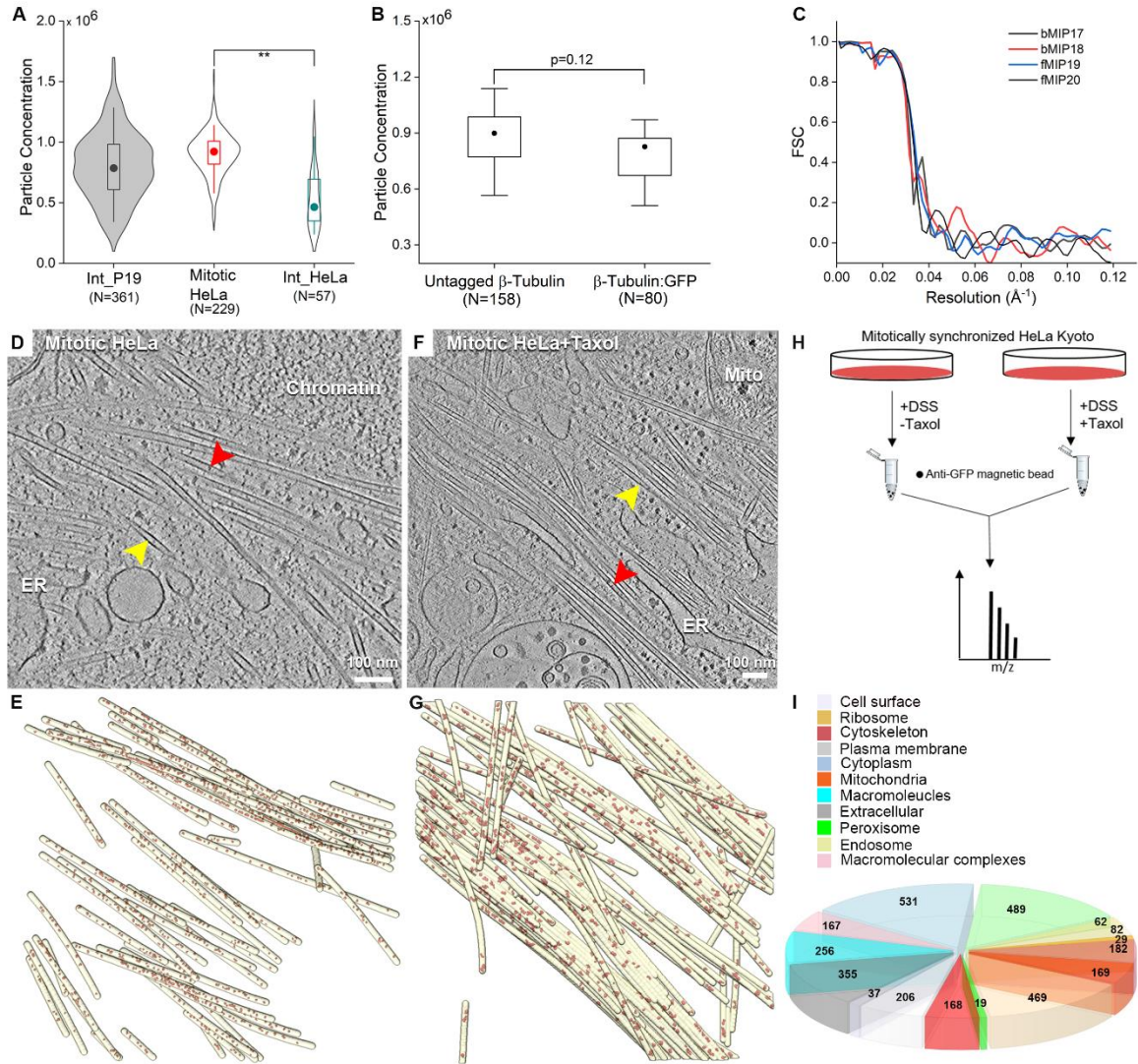
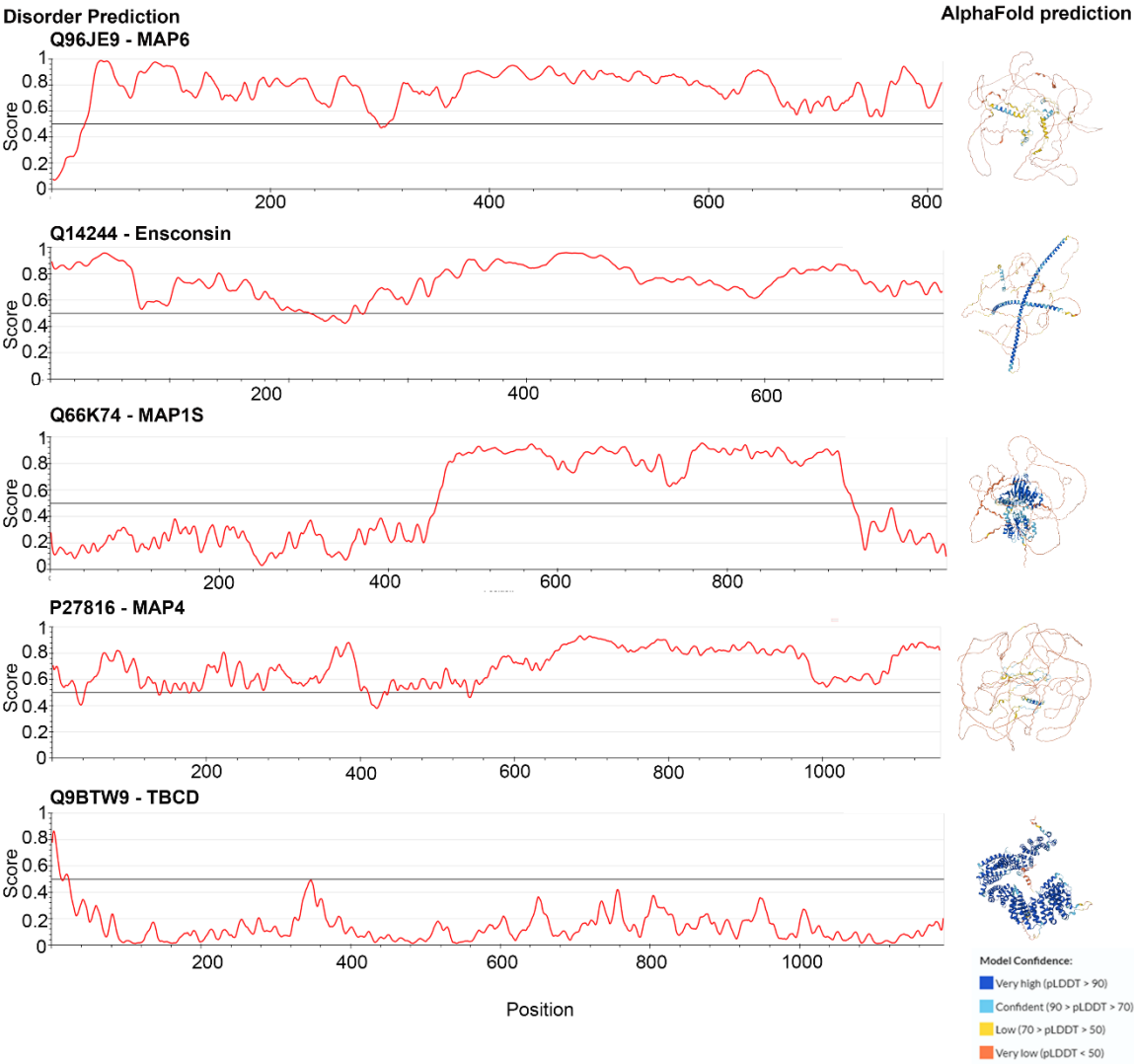


Fig. S8. Characterization of mitotic HeLa luminal particles. **A.** Quantification of the particle concentrations (particles/ μm^3 of luminal volume) in HeLa cells at different stages of cell cycle. For comparison, concentrations for P19 and mitotic HeLa from Fig.1I and 3F, respectively are replotted here. Median values are marked by a circle. Asterisks indicate Mann-Whitney test **: significance $p < 0.01$; N, number of MTs. **B.** Luminal particle concentration is unaffected by C-terminal GFP-tagging in mitotic HeLa cells. Two-sample unpaired t-test reveals insignificant difference ($p > 0.05$) between two cell types. **C.** FSC plots of the post-processed averages of mitotic HeLa MT luminal particles. 8.4 nm tomographic slices and 3D-surface rendering of MTs (yellow) and luminal particles (red) of **D, E.** control and **F, G,** Taxol-treated mitotic HeLa cell expressing GFP tagged β -tubulin. **H.** Experimental strategy for AP-MS-based identification of luminal particles from their fold reductions due to Taxol treatment. DSS: Disuccinimidyl suberate. **I.** Pie-chart shows distribution of cellular components based on gene-ontology (GO)-categorization of all the proteins identified in

544 the AP-MS proteomics. Numbers indicate number of proteins that belong to each subcategory. 168
545 proteins were found to be cytoskeleton related.
546



548
549
550
551
552
553
554
555
556
557
558

Fig. S9: Protein disorder prediction of selected MT-cytoskeleton related AP-MS hits. UniProt identifiers are indicated along with the protein IDs (human). Disorder prediction is obtained with IUPred3 server (45). Red lines indicate prediction score on the scale of 0 to 1. Threshold (black line) is set at a default value of 0.5. Scores above the threshold indicate disordered regions. Right panel shows AlphaFold2 (44) predicted structures of the proteins. Color coding indicate per-residue confidence score (pLDDT) on a scale between 0 and 100. All detected MAPs are predicted to be largely unstructured, whereas TBCD has a globular structure. For more comprehensive coverage of the highest AP-MS hits, see **Table S2**. Although we do not find MAP6, a suggested component of luminal particles in our AP-MS hits, it is included here for comparison.

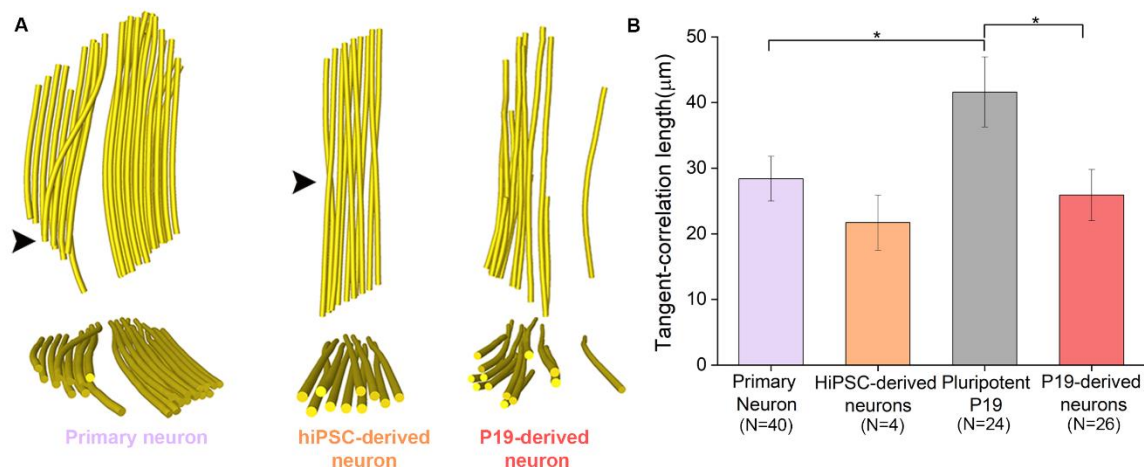
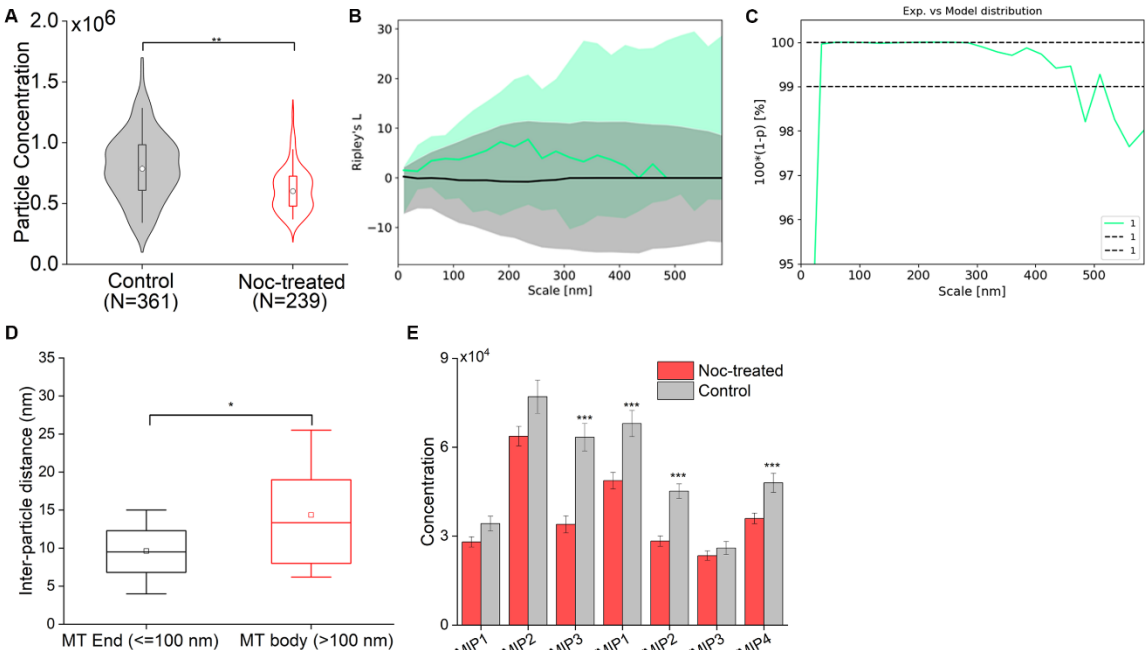


Fig. S10: MT curvature correlates with luminal particle concentration. **A.** Representative 3D rendering of MT bundles from a primary, hiPSC and P19-derived neuronal process. Top, x-y views, bottom, x-z views. Black arrowheads indicate MTs displaying curved trajectory. **B.** Quantification of MT curvatures. Bar graph representing mean tangent-correlation lengths (aL_p) of MTs in primary neurons, hiPSC-derived neurons, pluripotent P19 cells and P19-derived neurons. N, denotes number of tomograms analyzed. Error bar indicates SEM. Statistical significance * $p < 0.05$, obtained by two-sample t-test.

567

568



569

570

571

572

573

574

575

576

577

578

579

580

581

582

583

584

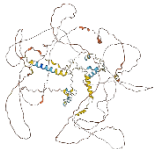

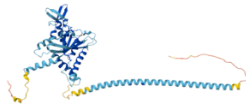
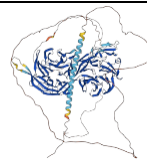
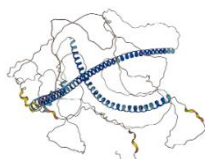
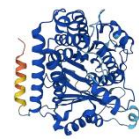
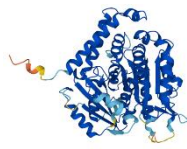
Fig. S11: Clustering of particles at open-ends of freshly polymerized MTs in pluripotent P19 cells. **A.** Quantification of particle concentrations (particles/ μm^3 of luminal volume) in control and freshly polymerized MTs of pluripotent P19 cells. Statistical significance by Mann-Whitney test $**p<0.01$; N, number of MTs. Concentration for P19 from Fig.1I is replotted here. **B.** Bivariate Ripley's L function for the particles clusters found at the MT open-ends: experimental (green) vs. random simulated null-model (black). Lines represent the median and shaded areas the IC [5, 95]%. **C.** One-sided Welch test for comparison between the experimental mean (green line) and the simulated one for every scale. Black dashed lines demarcated region indicate area of 99% significance. At a distance >200 nm, significance drops, indicating clustering (higher density than random null-model) only occurs at the open end. **D.** Boxplot shows distance between the particles located within 100 nm from the MT open end (black box) and further away (red box). Line indicate median and small rectangle denotes mean value. N=5 MTs, statistical significance by two sample t-test, $p<0.05$. **E.** Concentrations (particles/ μm^3 of luminal volume) of the indicated class averages in control and Noc-treated pluripotent P19 cells. Error bar indicates SEM. Statistical significance $***p<0.001$, obtained by two-sample t-test.

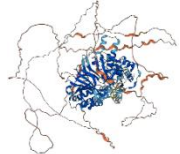
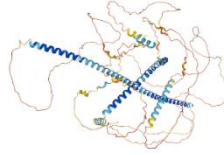
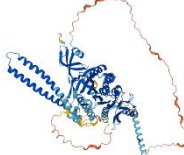
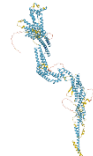
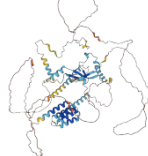
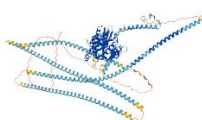
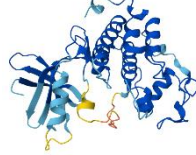
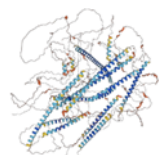
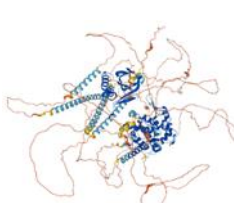
585 **Table S1.** Summary of the data sets from different cell types used for STA.

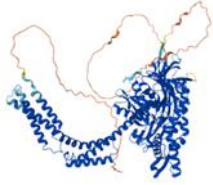
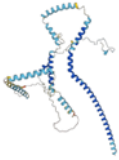
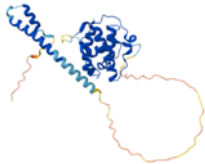
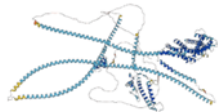

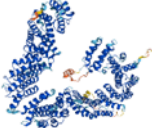
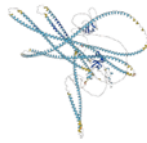
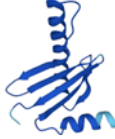
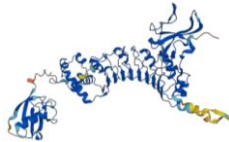
	<i>Murine P19 cells*</i>	<i>Human iPSC derived neuron</i>	<i>Rat primary neuron</i>	<i>Mitotic HeLa cells</i>	<i>Global resolution FSC@0.143 (Å)</i>
#VPP tomograms	46	8	-	12	-
#Defocus tomograms	35	-	60	-	-
#subtomograms	44,944	8635	50910	-	-
#bMIP1 subtomograms	4411	-	-	-	21.05
#bMIP2 subtomograms	4466	-	-	-	16.69
#bMIP3 subtomograms	3224	-	-	-	21.46
#bMIP4 subtomograms	1519	-	-	-	24.45
#fMIP1 subtomograms	3825	-	-	-	20.12
#fMIP2 subtomograms	2536	-	-	-	23.87
#fMIP3 subtomograms	1653	-	-	-	26.39
#fMIP4 subtomograms	3060	-	-	-	25.91
#fMIP5 subtomograms	-	-	2567	-	25.25
#fMIP6 subtomograms	-	-	2580	-	26.18
#fMIP7 subtomograms	-	-	3126	-	20.92
#fMIP8 subtomograms	-	-	1021	-	32.26
#fMIP9 subtomograms	-	-	2621	-	22.03
#fMIP10 subtomograms	-	-	1126	-	26.81
#fMIP11 subtomograms	-	-	2362	-	28.67
#fMIP12 subtomograms	-	-	5071	-	26.60
#fMIP13 subtomograms	-	2151	-	-	26.46
#fMIP14 subtomograms	-	380	-	-	30.86
#fMIP15 subtomograms	-	3738	-	-	24.51
#fMIP16 subtomograms	-	779	-	-	27.1
# bMIP17 subtomograms	-	-	-	2498	25.6
# bMIP18 subtomograms	-	-	-	1918	25.6
# fMIP19 subtomograms	-	-	-	1270	25.6
# fMIP20 subtomograms	-	-	-	699	28.3
#80S Ribosome subtomograms	4723	-	-	-	17.27
# MT subtomograms	-	-	-	34906	8.19


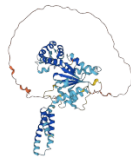

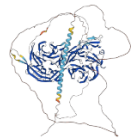
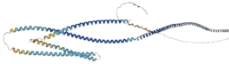
586 *For pluripotent and differentiated P19 cells, both VPP and defocus data were obtained and
587 processed separately.

588 **Table S2.** Top hits of MT-cytoskeleton related proteins obtained from the AP-MS experiment with
589 their AlphaFold-2 predicted structures. An estimate of the structural disorder determined from
590 IUPred3 server is also included. Color coding of AlphaFold-2 predicted structures indicate per-
591 residue confidence score (pLDDT) on a scale between 0 and 100. Please see Fig. S9 for detail and
592 **MS data table.** This table is not exhaustive.

Hits	UniProt ID	Function	Mol. Wt. (kDa)	Structural disorder (IUPred3)	Predicted structure (AlphaFold-2)
*Microtubule-associated protein 6 (MAP6)	Q96JE9	MT stabilization	86.5	Highly disordered	
Microtubule-associated protein 4 (MAP4)	P27816	MT stabilization	121	Highly disordered	
Septin6	Q14141	cytokinesis	49.7	Structured	
Echinoderm microtubule-associated protein 4 (EML4)	Q9HC35	MT stabilization	108.9	Partially disordered	
Ensconsin	Q14244	MT stabilization	84	Highly disordered	
Tubulin beta-6	Q13509	MT constituent	50.4	Structured	
Tubulin alpha 4A	P68366	MT constituent	49.9	Structured	

Microtubule-associated protein 1S (MAP1S)	Q66K74	MT stabilization	112.2	Partially disordered	
Microtubule-associated protein 7 (MAP7D1)	Q3KQU3	MT stabilization	92.8	Highly disordered	
Kinesin-like protein KIF2A	O00139	spindle dynamics during mitosis	79.9	Partially disordered	
Cytoplasmic Dynein 1 Heavy chain 1	A0A7P0TBC9	Trafficking	136.9	Structured	
Cytoskeleton-associated protein 2 (CKAP2)	Q8WWK9	MT stabilization	76.9	Partially disordered	
Kinesin 1 heavy chain	Q12840	Traffic	117.3		
Cyclin dependent kinase 1	P06493	cell cycle	34	Structured	
Microtubule cross-linking factor 1	Q9Y4B5	MT dynamics regulation	209	Partially disordered	
CAMSAP3	Q9P1Y5	MT organizer	134.7	Highly disordered	

Heat Shock protein 105 kDa	Q92598	nucleotide-exchange factor	96	structured	
Dynactin subunit2	Q13561	Trafficking	44.2	Structured	
MAPRE1	Q15691	MT stabilization	29.9	Partially disordered	
Dynactin subunit 1	Q14203	Trafficking	141.6	Structured	
Tubulin Binding Chaperone-A	O75347	Tubulin proteostasis	12.8	Structured	
Tubulin Binding Chaperone-D	Q9BTW9	Tubulin proteostasis	110	Structured	
CLIP1	P30622	MT polymerization	162.2	Partially disordered	
Dynein light chain roadblock-type 1	Q9NP97	Cargo recruitment	10.9	Structured	
Tubulin Binding Chaperone-E	Q15813	Tubulin proteostasis	59.3	Structured	

Stathmin	P16949	MT destabilization	17.3	Structured	
Katanin	O75449	MT destabilization	56	Partially disordered	
Dynein Light chain 1	P63167	Trafficking	10.3	Structured	
EML4	Q9HC35	MT stabilization	108.9	Partially disordered	
Cytoskeleton-associated protein 4	Q9HC35	ER-MT interaction mediator	66	Structured	

*MAP6 is neuron-specific. It is included here only for comparison.

Supplemental videos titles and legends

Movie S1. Tomographic slices of a primary hippocampal neuronal process showing the ultrastructure of the MT cytoskeleton. Related to Figure 1A, S1A. Color coding, MT: yellow, membrane: grey and luminal particles: red.

Movie S2. Tomographic slices of a pluripotent P19 cellular process showing the ultrastructure of the cytoplasm containing MTs. Related to Figure 1C. Color coding, MT: yellow, membrane: grey and luminal particles: red.

Movie S3. Tomographic slices of a hiPSC-derived neuronal process showing the ultrastructure of the MT cytoskeleton. Related to Figure 1E. Color coding, MT: yellow, membrane: grey and luminal particles: red.

Movie S4. Tomographic slices of a Taxol-treated pluripotent P19 cellular process showing the ultrastructure of the cytoplasm containing MTs. Related to Figure S7C. Color coding, MT: yellow and luminal particles: red.

Movie S5. Tomographic slices of a pluripotent P19 cellular process showing freshly polymerized MTs after Nocodazole treatment and washout. Related to Figure 6I. Color coding, MT: yellow and luminal particles: red.

Legend of the MS Data table: Numerical data (-log P versus Student's T-test difference) plotted as a volcano plot in Figure 3H.

SI References

1. C. Papantoniou, *et al.*, Munc13- and SNAP25-dependent molecular bridges play a key role in synaptic vesicle priming. *Sci. Adv.* **9**, eadf6222 (2023).
2. S. Chakraborty, J. Mahamid, W. Baumeister, Cryoelectron Tomography Reveals Nanoscale Organization of the Cytoskeleton and Its Relation to Microtubule Curvature Inside Cells. *Structure* **28**, 991-1003.e4 (2020).
3. Y. Zhang, *et al.*, Rapid single-step induction of functional neurons from human pluripotent stem cells. *Neuron* **78**, 785–798 (2013).
4. S.-M. Ho, *et al.*, Rapid Ngn2-induction of excitatory neurons from hiPSC-derived neural progenitor cells. *Methods* **101**, 113–124 (2016).
5. M. Toro-Nahuelpan, *et al.*, Tailoring cryo-electron microscopy grids by photo-micropatterning for in-cell structural studies. *Nat. Methods* **17**, 50–54 (2020).
6. J. Mahamid, *et al.*, Visualizing the molecular sociology at the HeLa cell nuclear periphery. *Science* **351**, 969–972 (2016).
7. Y. Fukuda, U. Laugks, V. Lučić, W. Baumeister, R. Danev, Electron cryotomography of vitrified cells with a Volta phase plate. *J. Struct. Biol.* **190**, 143–154 (2015).
8. D. N. Mastronarde, Automated electron microscope tomography using robust prediction of specimen movements. *J. Struct. Biol.* **152**, 36–51 (2005).
9. W. J. H. Hagen, W. Wan, J. A. G. Briggs, Implementation of a cryo-electron tomography tilt-scheme optimized for high resolution subtomogram averaging. *J. Struct. Biol.* **197**, 191–198 (2017).
10. S. Khavnekar, P. Erdmann, W. Wan, TOMOMAN: Streamlining Cryo-electron Tomography and Subtomogram Averaging Workflows Using TOMOgram MANager. *Microsc. Microanal.* **29**, 1020–1020 (2023).
11. S. Q. Zheng, *et al.*, MotionCor2: anisotropic correction of beam-induced motion for improved cryo-electron microscopy. *Nat. Methods* **14**, 331–332 (2017).
12. K. Zhang, Gctf: Real-time CTF determination and correction. *J. Struct. Biol.* **193**, 1–12 (2016).
13. A. Rohou, N. Grigorieff, CTFFIND4: Fast and accurate defocus estimation from electron micrographs. *J. Struct. Biol.* **192**, 216–221 (2015).
14. B. Turoňová, F. K. M. Schur, W. Wan, J. A. G. Briggs, Efficient 3D-CTF correction for cryo-electron tomography using NovaCTF improves subtomogram averaging resolution to 3.4 Å. *J. Struct. Biol.* **199**, 187–195 (2017).
15. D. Tegunov, P. Cramer, Real-time cryo-electron microscopy data preprocessing with Warp. *Nat. Methods* **16**, 1146–1152 (2019).
16. J. R. Kremer, D. N. Mastronarde, J. R. McIntosh, Computer visualization of three-

dimensional image data using IMOD. *J. Struct. Biol.* **116**, 71–76 (1996).

17. Y. T. Liu, *et al.*, Isotropic reconstruction for electron tomography with deep learning. *Nat. Commun.* **13**, 1–17 (2022).

18. A. Martinez-Sanchez, *et al.*, Template-free detection and classification of membrane-bound complexes in cryo-electron tomograms. *Nat. Methods* **17**, 209–216 (2020).

19. D. Comaniciu, P. Meer, Mean shift: A robust approach toward feature space analysis. *IEEE Trans. Pattern Anal. Mach. Intell.* **24**, 603–619 (2002).

20. J. Zivanov, *et al.*, New tools for automated high-resolution cryo-EM structure determination in RELION-3. *Elife* **7:e42166** (2018).

21. E. F. Pettersen, *et al.*, UCSF Chimera - A visualization system for exploratory research and analysis. *J. Comput. Chem.* **25**, 1605–1612 (2004).

22. W. Wan, S. Khavnekar, J. Wagner, P. Erdmann, W. Baumeister, STOPGAP: A Software Package for Subtomogram Averaging and Refinement. *Microsc. Microanal.* **26**, 2516–2516 (2020).

23. W. Wan, S. Khavnekar, J. Wagner, STOPGAP: an open-source package for template matching, subtomogram alignment and classification. *Acta Crystallogr. Sect. D Struct. Biol.* **80**, 336–349 (2024).

24. K. Qu, *et al.*, Structure and architecture of immature and mature murine leukemia virus capsids. *Proc. Natl. Acad. Sci. U. S. A.* **115**, E11751–E11760 (2018).

25. H. Li, D. J. DeRosier, W. V. Nicholson, E. Nogales, K. H. Downing, Microtubule Structure at 8 Å Resolution. *Structure* **10**, 1317–1328 (2002).

26. E. Nogales, M. Whittaker, R. A. Milligan, K. H. Downing, High-resolution model of the microtubule. *Cell* **96**, 79–88 (1999).

27. J. V. Ribeiro, *et al.*, QwikMD — Integrative Molecular Dynamics Toolkit for Novices and Experts. *Sci. Rep.* **6**, 26536 (2016).

28. S. Nickell, *et al.*, TOM software toolbox: acquisition and analysis for electron tomography. *J. Struct. Biol.* **149**, 227–234 (2005).

29. R. Englmeier, S. Pfeffer, F. Förster, Structure of the Human Mitochondrial Ribosome Studied In Situ by Cryoelectron Tomography. *Structure* **25**, 1574-1581.e2 (2017).

30. H. Khatter, A. G. Myasnikov, S. K. Natchiar, B. P. Klaholz, Structure of the human 80S ribosome. *Nature* **520**, 640–645 (2015).

31. T. Hrabe, *et al.*, PyTom: A python-based toolbox for localization of macromolecules in cryo-electron tomograms and subtomogram analysis. *J. Struct. Biol.* **178**, 177–188 (2012).

32. W. Jiang, *et al.*, A transformation clustering algorithm and its application in polyribosomes structural profiling. *Nucleic Acids Res.* **50**, 9001–9011 (2022).

33. A. Martinez-Sanchez, W. Baumeister, V. Lučić, Statistical spatial analysis for cryo-electron tomography. *Comput. Methods Programs Biomed.* **218**, 106693 (2022).

34. E. F. Pettersen, *et al.*, UCSF ChimeraX: Structure visualization for researchers, educators, and developers. *Protein Sci.* **30**, 70–82 (2021).
35. L. Lamm, *et al.*, MemBrain v2: an end-to-end tool for the analysis of membranes in cryo-electron tomography. *bioRxiv* 2024.01.05.574336 (2024).
36. A. Cook, *et al.*, The structure of the nuclear export receptor Cse1 in its cytosolic state reveals a closed conformation incompatible with cargo binding. *Mol. Cell* **18**, 355–367 (2005).
37. S. Nithianantham, *et al.*, Tubulin cofactors and Arl2 are cage-like chaperones that regulate the soluble $\alpha\beta$ -tubulin pool for microtubule dynamics. *Elife* **4**:e08811 (2015).
38. B. L. Lytle, *et al.*, Solution Structure of a Ubiquitin-like Domain from Tubulin-binding Cofactor B. *J. Biol. Chem.* **279**, 46787–46793 (2004).
39. M. Serna, *et al.*, The structure of the complex between α -tubulin, TBCE and TBCB reveals a tubulin dimer dissociation mechanism. *J. Cell Sci.* **128**, 1824–1834 (2015).
40. M. Hothorn, *et al.*, Structural basis of steroid hormone perception by the receptor kinase BRI1. *Nature* (2011). <https://doi.org/10.1038/nature10153>.
41. I. Poser, *et al.*, BAC TransgeneOmics: A high-throughput method for exploration of protein function in mammals. *Nat. Methods* **5**, 409–415 (2008).
42. J. Cox, M. Mann, MaxQuant enables high peptide identification rates, individualized p.p.b.-range mass accuracies and proteome-wide protein quantification. *Nat. Biotechnol.* **26**, 1367–1372 (2008).
43. S. Tyanova, *et al.*, The Perseus computational platform for comprehensive analysis of (prote)omics data. *Nat. Methods* (2016).
44. J. Jumper, *et al.*, Highly accurate protein structure prediction with AlphaFold. *Nature* **596**, 583–589 (2021).
45. G. Erdos, M. Pajkos, Z. Dosztányi, IUPred3: Prediction of protein disorder enhanced with unambiguous experimental annotation and visualization of evolutionary conservation. *Nucleic Acids Res.* **49**, W297–W303 (2021).
46. H. E. Foster, C. Ventura Santos, A. P. Carter, A cryo-ET survey of microtubules and intracellular compartments in mammalian axons. *J. Cell Biol.* **221**, e202103154 (2022).
47. S. H. W. Scheres, Amyloid structure determination in RELION -3.1. *Acta Crystallogr. Sect. D Struct. Biol.* **76**, 94–101 (2020).